Journal of Operation and Automation in Power Engineering

Vol. XX, No. XX, XXXX, Pages: XXXX (Proofed)

http://joape.uma.ac.ir

Research Paper

Single-Switch Dual-String Non-Isolated Constant-Current LED Driver

Mitra Sarhangzadeh [1], *Jaber Fallah Ardashir* [1,*], *Aydin Mohammad Ogly* [1], and *Hossein Khoun Jahan* [2]

[1]*Department of Electrical Engineering, Ta.C., Islamic Azad University, Tabriz, Iran.*
[2]*Azarbaijan Regional Electric Company, Tabriz, Iran.*

Abstract— *A compact single-switch, dual-string, non-isolated constant-current LED driver is proposed to address the tradeoff between power quality, current regulation, and lifetime in integrated single-stage drivers, where electrolytic dc-link buffering and increased component count often limit reliability and cost. The topology integrates boost power factor correction and buck current regulation in one switching stage, provides automatic per-string current sharing, and eliminates electrolytic bulk capacitance by transferring energy buffering to the output using non-electrolytic capacitors. A small-signal averaged model is derived to design cascaded inner–outer proportional–integral control loops for input-current shaping and dual-string current regulation. A 110 W prototype (two strings, 39 V/1.42 A per string) operating from 180–265 V_{AC} at 20 kHz achieves 94% peak efficiency, power factor ≈ 0.97, input-current THD ≈ 5%, and 13% LED current ripple with negligible perceptible flicker. The results confirm robust regulation under mains and load variations, demonstrating suitability for compact, long-life street-lighting drivers.*

Keywords—Non-electrolytic capacitor, light flicker, low current ripple, high power factor, lifespan.

1. Introduction

Light-emitting diodes (LEDs) occupy a central position in modern lighting owing to their high luminous efficacy, long service life, compact form factor, and robustness to shock and vibration. In addition to efficiency, LEDs enable rich color control and fast dynamic response, which makes them attractive for street, architectural, and industrial applications. Because lighting still represents a substantial portion of electricity demand, improving luminaire efficiency remains an effective lever for reducing energy use and emissions, and this places particular emphasis on the power-electronic interface of the luminaire [1], where conversion losses and reliability limitations are largely determined. Ref. [2] further highlights that system-level efficiency and power-quality compliance are strongly coupled to the driver design and operating conditions. The LED driver not only converts ac mains to a regulated dc output but must also enforce accurate constant-current regulation to prevent thermal runaway and color shifts; this requirement is emphasized in [3], which discusses current-regulation needs under LED electrical nonlinearity. In addition, flicker mitigation and input-side power-quality constraints are highlighted in [4], which motivates the need for coordinated control of both output ripple and grid-side current quality. Consequently, the key technical objectives of an ideal driver include high conversion efficiency, near-unity power factor with low input-current harmonics, low output current ripple, robust dimming capability, and long-term reliability. A critical lifetime-related constraint is the energy-buffer capacitor technology; [5] identifies reliability limitations in luminaire power stages, while [5] explicitly discusses the lifetime bottleneck associated with electrolytic capacitors in offline drivers, motivating capacitor-reduced or electrolytic-free implementations.

Proper power factor correction is a fundamental requirement for converters tied to the ac grid. An LED driver connected directly to the mains must not degrade grid power quality or inject significant current harmonics; therefore, it should incorporate an active power-factor-correction (PFC) stage or an equivalent input-current shaping strategy. The need for near-unity power factor and low total harmonic distortion (THD) is discussed in [2] from a grid-interface perspective. Achieving this objective requires the input current to be controlled to track the mains voltage with an appropriate bandwidth and modulation strategy, while also accounting for practical constraints such as switching losses and electromagnetic interference (EMI). Ref. [5] discusses these practical tradeoffs and explains why meeting power-quality requirements must be balanced against efficiency, thermal stress, and reliability considerations. The input to the LED driver is the rectifier output (dc link). To achieve near-unity power factor on the ac side, it is undesirable to place a large bulk capacitor directly at the rectifier output because a stiff dc-link decouples the input current from the mains and prevents the line current from tracking the mains voltage. Omitting that capacitor, however, produces a large low-frequency ripple on the rectified voltage; because LED current depends nonlinearly on the LED string voltage, even moderate voltage ripple can generate disproportionately large current ripple and visible flicker, as discussed in [6]. A practical remedy is to shift the required energy buffering away from the rectifier dc link and toward the output so that the LED voltage/current can be smoothed locally. With respect

Received: 27 Sept. 2025
Revised: 20 Dec. 2025
Accepted: 01 Jan. 2026
*Corresponding author:
E-mail: j.fallah@iau.ac.ir (J. Fallah Ardashir)
DOI: 10.22098/joape.2026.18447.2439

to capacitor technology, [7] explains that electrolytic capacitors offer high capacitance density but limited lifetime and weaker high-temperature reliability, whereas film and ceramic capacitors provide longer service life and better stability, making them preferable for long-lived luminaires. Building on this motivation, [8] presents the design concept of combining input-current shaping with output-side regulation in a way that reduces dependency on life-limiting bulk electrolytic capacitors. In this context, an ideal driver is expected to produce a sinusoidal, near-unity ac-side current and a low-ripple constant output current with compact component count, high efficiency, and long-term reliability at reasonable cost; these combined objectives are emphasized in [9] from a performance standpoint and further reinforced in [10] from a practical implementation viewpoint.

LED drivers are commonly classified as single-stage, two-stage, and integrated architectures. In a single-stage design, a single power-processing stage performs both output-current regulation and input-current shaping; this classification and its inherent constraints are discussed in [11]. Although single-stage solutions can reduce parts count and cost, they often rely on relatively large electrolytic energy buffering at the dc link or output to suppress low-frequency ripple, which can reduce lifetime and thermal robustness. To alleviate this tradeoff, [12] proposes separating the PFC and regulation functions into a multi-block structure to improve controllability and ripple management. Ref. [13] reports that distributing the energy-buffer requirement across stages can reduce the need for large electrolytic capacitors and improve reliability. Ref. [14] further motivates integrated or function-merged approaches as a compromise that targets both reliability and component-count reduction.

To overcome the shortcomings of single-stage drivers, two-stage architectures are widely adopted, where the first stage implements input PFC and the second stage performs precise output-current regulation. This separation enables improved controllability and allows smaller energy-storage elements to be placed where they are most effective for ripple suppression and dynamic regulation. The principal drawback is increased parts count, board area, and cost associated with separate converter stages. To mitigate these penalties, integrated driver topologies reuse components across stages or merge functions to reduce complexity while retaining the advantages of separated PFC and output regulation; the motivation for integration is discussed in [6] from a ripple/flicker perspective, while [15] presents integration as a component-reduction strategy that targets compactness and manufacturability.

For multi-string LED drivers, a dominant lifetime and performance concern is current imbalance between strings. Ref. [16] highlights that mismatch in forward voltage, wiring, and thermal drift can produce unequal current sharing that accelerates aging in the overstressed string. Ref. [17] discusses that while passive balancing approaches can be simple and robust, they often waste power or provide limited accuracy, whereas active balancing improves regulation at the expense of additional sensing, control complexity, and potential stability interactions. Ref. [18] further details that multi-string implementations also complicate EMI filtering, thermal management, and fault handling, which must be addressed to preserve reliability. These tradeoffs motivate topologies that achieve accurate current sharing with minimal additional components and losses. In this direction, [19] motivates dual-string regulation strategies to maintain per-string current equality under mismatch conditions, and [20] further supports the need for compact architectures that maintain power quality and reliability without adding multiple power stages.

In this paper, we propose a compact, single-switch, dual-string non-isolated constant-current LED driver that combines high input power factor, low output-current ripple, and elimination of electrolytic bulk capacitors with automatic per-string current sharing and the flexibility to support unequal LED-string lengths. The topology employs a unified switching stage and a linear cascaded control scheme to regulate both the LED currents and the grid-side power factor. The concept is validated through detailed simulations and a hardware prototype rated at 110 W total output; measured results show high conversion efficiency (≈94–95%), near-unity power factor (PF ≈ 0.97), low input current THD (≈5%), and reliable operation across a wide input range (180–265 V_{AC}). These results demonstrate the proposed driver's suitability for compact, long-life, high-performance lighting applications such as street luminaires.

2. Mode analysis of the proposed LED driver

As shown in Fig. 1, the proposed two-string LED driver integrates boost and buck functions for each LED string while sharing a single power switch 'S', yielding a compact and low-parts-count topology. The converter's switching cycle is divided into four principal modes (I–IV), depicted in Fig. 2 and summarized in Table I and Table II; mode III bifurcates into two boundary subcases (III-1 and III-2) depending on the instantaneous inductor currents and the relative energy stored in L_m versus L_1/L_2. A representative interval $t_0 - t_4$ is used below to explain the detailed dynamic behavior; 'd' denotes the duty ratio of power switch 'S'.

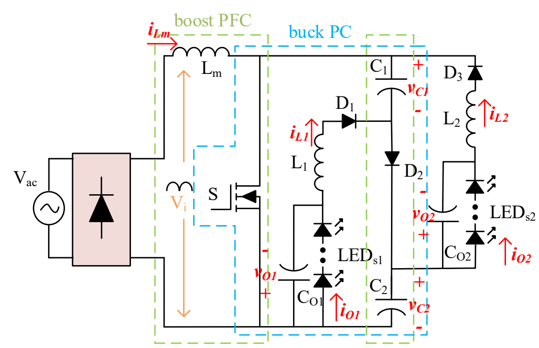

Fig. 1. Proposed two-string LED driver.

As shown in Fig. 2-(a), mode I (S=on): when power switch 'S' is turned on, the magnetizing inductor L_m is energized from the input source while energy is also transferred to the secondary inductors L_1 and L_2 through diodes D_1 and D_3. During this interval the diode D_2 remains reverse-biased by the summed capacitor voltage (V_{C1}+V_{C2}), preventing back-flow into the capacitor network. The currents i_{Lm}, i_{L1} and i_{L2} rise according to their respective volt-second balances.

Mode II (S=off, discharge mode): according to Fig. 2-(b), turning off the power switch 'S' causes L_m, L_1 and L_2 to release stored energy. D_1 and D_3 continue to conduct the LED string currents (i_{L1} and i_{L2}) into the loads, while the voltage at the L_m node reverses and forward-biases D_2 so that L_m can return energy toward the capacitor network. This interval implements the boost action for the shared stage while simultaneously allowing the string inductors to supply the LEDs.

Mode III (boundary subcases) shown in Figs. 2-(c) and 2-(d): with power switch 'S' still off and D_2 conducting, two possible sequences follow depending on which inductor currents reach zero first. In III-1 mode (Fig. 2-(c)), i_{L1} and i_{L2} decay to zero before i_{Lm}; the residual i_{Lm} therefore flows through D_2 and charges C_1 and C_2, raising their voltages and storing energy for the next cycle. In III-2 mode (Fig. 2-(d)), i_{Lm} reaches zero first while i_{L1}/i_{L2} remain finite; in that case all diodes D_1, D_2 and D_3 can be concurrently forward-biased and the remaining energy in L_1/L_2 is delivered directly to the LED strings and capacitor network. These subcases represent different energy-transfer paths and define the boundary conditions for inductor sizing and control timing.

Mode IV (dead interval), illustrated in Fig. 2-(e): in this final stage, all semiconductor devices are non-conducting for a brief period. This controlled dead-time establishes a zero-current interval, suppresses undesired circulating currents, and assists in clamping the node voltages to stable levels before the next switching cycle begins. The duration and occurrence of each mode (particularly which III subcase occurs) are sensitive to the relative inductances, capacitor sizes and load currents; therefore, selecting L_m, L_1 and L_2 and designing the capacitor bank (C_1, C_2) are critical to ensure desired current-sharing, low output ripple, soft transitions and to avoid undesired discontinuous behavior. Control-wise, the topology supports per-string regulation via measured i_{L1} and i_{L2} and a duty-cycle schedule for S that balances power factor, ripple and dimming requirements.

Table 1. Operating modes. Mode I, II, III-1, IV.

Time interval	Description	Intervals	Mode
dT	S, D_1, D_3: on	t_0–t_1	I
d_2T	D_1, D_2, D_3: on	t_1–t_2	II
$(d_1-d_2)T$	D_2: on	t_2–t_3	III-1
$(1-d-d_1)T$	–	t_4–t_5	IV

Table 2. Operating modes. Mode I, II, III-2, IV.

Time interval	Description	Intervals	Mode
dT	S, D_1, D_3: on	t_0–t_1	I
d_1T	D_1, D_2, D_3: on	t_1–t_2	II
$(d_2-d_1)T$	D_1, D_2, D_3: on	t_3–t_4	III-2
$(1-d-d_2)T$	–	t_4–t_5	IV

3. Dynamic modeling and linear control for the proposed LED driver

In this section, the proposed LED driver topology is analyzed using the state-space modeling framework. Based on the switching intervals summarized in Tables 1 and 2 and the operating waveforms shown in Fig. 3, the averaged steady-state models are derived for the two possible operating sequences: (i) modes I, II, III-1, IV and (ii) modes I, II, III-2, IV. These derivations result in the state-space equations expressed in Eqs. (1) and (2).

$$\mathbf{x}' = \mathbf{A}\mathbf{x} + \mathbf{B}\mathbf{u}, \tag{1}$$

where,

$$\mathbf{x} = \begin{bmatrix} i_{Lm} & i_{L1} & i_{L2} & v_{C1} & v_{C2} & v_{O1} & v_{O2} & i_{O1} & i_{O2} \end{bmatrix}^T,$$
$$\mathbf{u} = \begin{bmatrix} V_i & V_{LED1} & V_{LED2} \end{bmatrix}.$$

with

$$A_{11} =$$

$$\begin{bmatrix} -\frac{d_1 r_d + d r_s}{L_m} & -\frac{d_2 r_d + d r_s}{L_m} & -\frac{d_2 r_d + d r_s}{L_m} \\ [2mm] -\frac{d_2 r_d + d r_s}{L_1} & -\frac{2d_2 r_d + d(r_d + r_s)}{L_1} & -\frac{d_2 r_d + d r_s}{L_1} \\ [2mm] -\frac{d_2 r_d + d r_s}{L_2} & -\frac{d_2 r_d + d r_s}{L_2} & -\frac{2d_2 r_d + d(r_d + r_s)}{L_2} \end{bmatrix}.$$

$$A_{12} = \begin{bmatrix} -\frac{d_1}{L_m} & -\frac{d_1}{L_m} & 0 \\ \frac{d}{L_1} & -\frac{d_2}{L_1} & -\frac{d+d_2}{L_1} \\ -\frac{d}{L_2} & \frac{d}{L_2} & 0 \end{bmatrix},$$

$$A_{13} = \begin{bmatrix} 0 & 0 & 0 \\ 0 & 0 & 0 \\ -\frac{d+d_2}{L_2} & 0 & 0 \end{bmatrix},$$

$$A_{21} = \begin{bmatrix} \frac{d_1}{C_1} & -\frac{d}{C_1} & \frac{d_2}{C_1} \\ \frac{d_1}{C_2} & \frac{d_2}{C_2} & -\frac{d}{C_2} \\ 0 & \frac{d+d_2}{C_{O1}} & 0 \end{bmatrix},$$

$$A_{22} = \begin{bmatrix} 0 & 0 & 0 \\ 0 & 0 & 0 \\ 0 & 0 & 0 \end{bmatrix}, \qquad A_{23} = \begin{bmatrix} 0 & 0 & 0 \\ 0 & 0 & 0 \\ 0 & -\frac{1}{C_{O1}} & 0 \end{bmatrix},$$

$$A_{31} = \begin{bmatrix} 0 & 0 & \frac{d+d_2}{C_{O2}} \\ 0 & 0 & 0 \\ 0 & 0 & 0 \end{bmatrix},$$

$$A_{32} = \begin{bmatrix} 0 & 0 & 0 \\ 0 & 0 & 0 \\ 0 & 0 & 0 \end{bmatrix}, \qquad A_{33} = \begin{bmatrix} 0 & 0 & -\frac{1}{C_{O2}} \\ \frac{1}{L_{O1}} & -\frac{R_{LED1}}{L_{O1}} & 0 \\ 0 & \frac{1}{L_{O2}} & -\frac{R_{LED2}}{L_{O2}} \end{bmatrix}.$$

Input matrix

The original input matrix is:

$$\mathbf{B} = \begin{bmatrix} B_1 \\ B_2 \\ B_3 \end{bmatrix},$$

where,

$$B_1 = \begin{bmatrix} \frac{d+d_1}{L_m} & 0 & 0 \\ 0 & 0 & 0 \\ 0 & 0 & 0 \end{bmatrix},$$

$$B_2 = \begin{bmatrix} 0 & 0 & 0 \\ 0 & 0 & 0 \\ 0 & 0 & 0 \end{bmatrix},$$

$$B_3 = \begin{bmatrix} 0 & 0 & 0 \\ 0 & -\frac{1}{L_{O1}} & 0 \\ 0 & 0 & -\frac{1}{L_{O2}} \end{bmatrix}.$$

$$\begin{bmatrix} \dot{i}_{Lm} \\ \dot{i}_{L1} \\ \dot{i}_{L2} \\ \dot{v}_{C1} \\ \dot{v}_{C2} \\ \dot{v}_{O1} \\ \dot{v}_{O2} \\ \dot{i}_{O1} \\ \dot{i}_{O2} \end{bmatrix} = \mathbf{A} \begin{bmatrix} i_{Lm} \\ i_{L1} \\ i_{L2} \\ v_{C1} \\ v_{C2} \\ v_{O1} \\ v_{O2} \\ i_{O1} \\ i_{O2} \end{bmatrix} + \mathbf{B} \begin{bmatrix} V_i \\ V_{LED1} \\ V_{LED2} \end{bmatrix} \tag{2}$$

$$\mathbf{A} = \begin{bmatrix} A_{11} & A_{12} & A_{13} \\ A_{21} & A_{22} & A_{23} \\ A_{31} & A_{32} & A_{33} \end{bmatrix}$$

Block definitions

$$A_{11} = \begin{bmatrix} -\frac{d_1 r_d + d r_s}{L_m} & -\frac{d_1 r_d + d r_s}{L_m} & -\frac{d_1 r_d + d r_s}{L_m} \\ -\frac{d_1 r_d + d r_s}{L_1} & -\frac{2d_2 r_d + d(r_d + r_s)}{L_1} & -\frac{d_2 r_d + d r_s}{L_1} \\ -\frac{d_1 r_d + d r_s}{L_2} & -\frac{d_2 r_d + d r_s}{L_2} & -\frac{2d_2 r_d + d(r_d + r_s)}{L_2} \end{bmatrix}$$

$$A_{12} = \begin{bmatrix} -\frac{d_1}{L_m} & -\frac{d_1}{L_m} & 0 \\ \frac{d}{L_1} & -\frac{d_2}{L_1} & -\frac{d+d_2}{L_1} \\ -\frac{d_2}{L_2} & \frac{d}{L_2} & 0 \end{bmatrix}$$

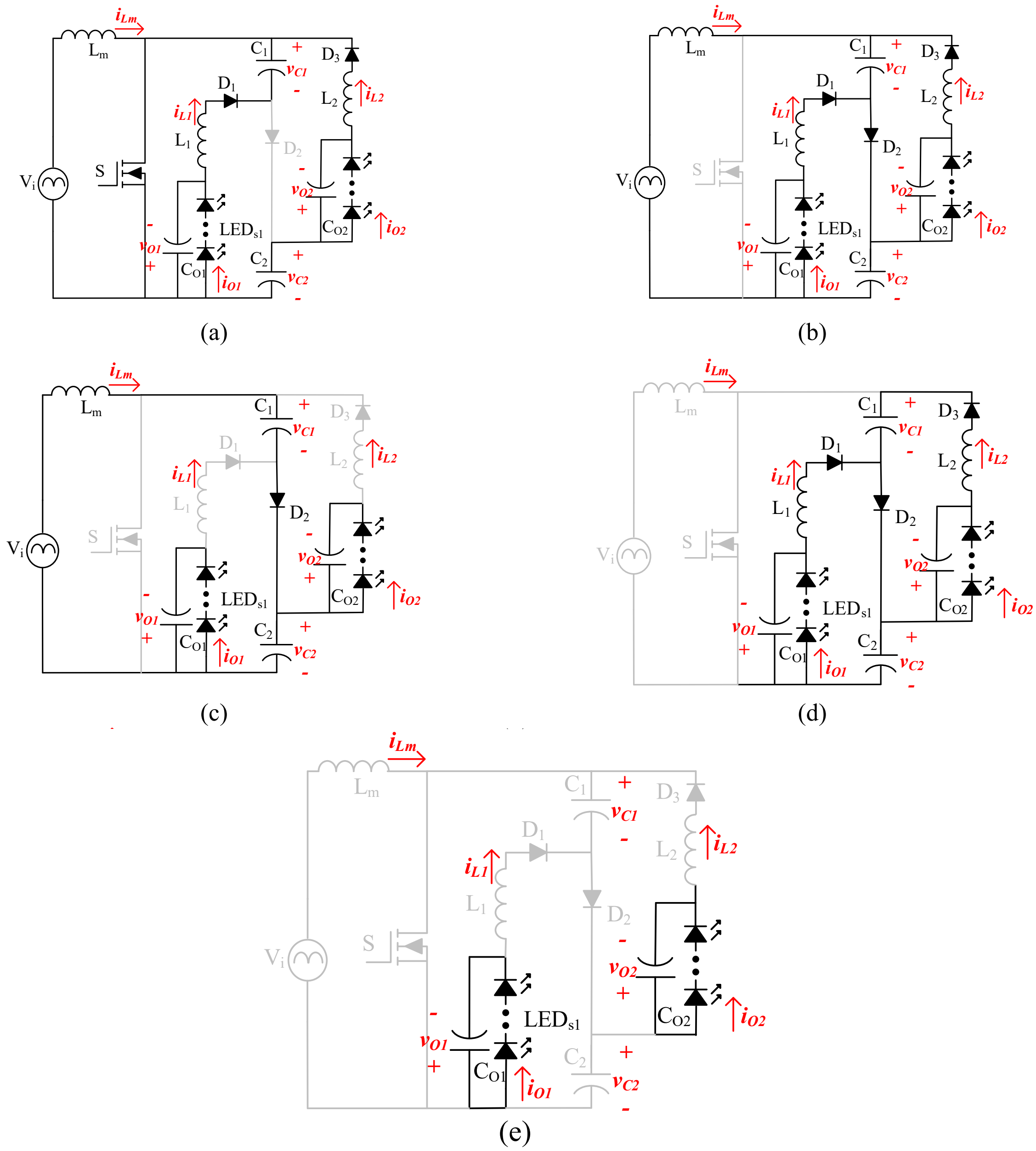

Fig. 2. Operating modes. (a) Mode I, (b) Mode II, (c) Mode III-1, (d) Mode III-2, and (e) Mode IV.

$$A_{13} = \begin{bmatrix} 0 & 0 & 0 \\ 0 & 0 & 0 \\ -\frac{d+d_2}{L_2} & 0 & 0 \end{bmatrix}$$

$$A_{21} = \begin{bmatrix} \frac{d_1}{C_1} & -\frac{d}{C_1} & \frac{d_2}{C_1} \\ \frac{d_1}{C_2} & \frac{d_2}{C_2} & -\frac{d}{C_2} \\ 0 & \frac{d+d_2}{C_{O1}} & 0 \end{bmatrix}$$

$$A_{22} = \begin{bmatrix} 0 & 0 & 0 \\ 0 & 0 & 0 \\ 0 & 0 & 0 \end{bmatrix}$$

$$A_{23} = \begin{bmatrix} 0 & 0 & 0 \\ 0 & 0 & 0 \\ 0 & -\frac{1}{C_{O1}} & 0 \end{bmatrix}$$

$$A_{31} = \begin{bmatrix} 0 & 0 & \frac{d+d_2}{C_{O2}} \\ 0 & 0 & 0 \\ 0 & 0 & 0 \end{bmatrix}$$

$$A_{32} = \begin{bmatrix} 0 & 0 & 0 \\ 0 & 0 & 0 \\ 0 & 0 & 0 \end{bmatrix}$$

$$A_{33} = \begin{bmatrix} 0 & 0 & -\frac{1}{C_{O2}} \\ \frac{1}{L_{O1}} & -\frac{R_{LED1}}{L_{O1}} & 0 \\ 0 & \frac{1}{L_{O2}} & -\frac{R_{LED2}}{L_{O2}} \end{bmatrix}$$

B matrix

$$\mathbf{B} = \begin{bmatrix} B_{11} & B_{12} \\ B_{21} & B_{22} \\ B_{31} & B_{32} \end{bmatrix}$$

Blocks

$$B_{11} = \begin{bmatrix} \frac{d+d_1}{L_m} & 0 & 0 \\ 0 & 0 & 0 \\ 0 & 0 & 0 \end{bmatrix}$$

$$B_{12} = \begin{bmatrix} \frac{V_i}{L_m} & \frac{V_i}{L_m} & 0 \\ \frac{-V_{O1}+V_{C1}}{L_1} & 0 & -\frac{V_{O1}+V_{C2}}{L_1} \\ \frac{-V_{O2}+V_{C2}}{L_2} & 0 & -\frac{V_{O2}+V_{C1}}{L_2} \end{bmatrix}$$

$$B_{21} = \begin{bmatrix} 0 & 0 & 0 \\ 0 & 0 & 0 \\ 0 & 0 & 0 \end{bmatrix}$$

$$B_{22} = \begin{bmatrix} \frac{-i_{L1}+i_{L2}}{C_1} & \frac{i_{Lm}}{C_1} & 0 \\ -\frac{i_{L2}}{C_2} & \frac{i_{Lm}}{C_2} & \frac{i_{L1}}{C_2} \\ \frac{i_{L1}}{C_{O1}} & 0 & \frac{i_{L1}}{C_{O1}} \end{bmatrix}$$

$$B_{31} = \begin{bmatrix} 0 & 0 & 0 \\ 0 & \frac{1}{L_{O1}} & 0 \\ 0 & 0 & -\frac{1}{L_{O2}} \end{bmatrix}$$

$$B_{32} = \begin{bmatrix} \frac{i_{L2}}{C_{O2}} & 0 & \frac{i_{L2}}{C_{O2}} \\ 0 & 0 & 0 \\ 0 & 0 & 0 \end{bmatrix}$$

The matrices in Eqs. (1) and (2) explicitly describe the dynamic behavior of the system in terms of the inductor currents, capacitor voltages, and output states, while incorporating the duty ratios ‘d’, ‘d_1’, and ‘d_2’. The distinction between Eqs. (1) and (2) corresponds to whether mode III occurs as submode III-1 or III-2, depending on which inductor current reaches zero first in discontinuous conduction mode. In these formulations, r_d and r_s represent the on-state resistances of the diodes and the main switch, respectively. For analytical simplification, the ideal case is considered with rd = rs = 0, and the passive components are assumed to be symmetric: $r_d = r_s = 0$, $L_1 = L_2 = L$, $C_1 = C_2 = C$, $L_{O1} = L_{O2} = L_O$, and $C_{O1} = C_{O2} = C_O$. Under these assumptions, the steady-state dc relationships can be compactly expressed as in Eq. (3). Eq. (3) reveals two important characteristics:

1. Equal output currents: $i_{O1} = i_{O2}$, ensuring current balance between the two output channels without auxiliary control circuitry.
2. Unequal output voltages: (3) indicating that the total output voltage depends on the duty ratios, while individual voltages across V_{O1} and V_{O2} can differ.

This feature is highly beneficial in LED applications, as it allows different numbers of LEDs to be connected in each string while maintaining identical current regulation. Consequently, the driver can support non-uniform LED loads, offering both design flexibility and robustness against LED forward-voltage mismatches.

$$\begin{aligned} & i_{O_1} = i_{O_2} \\ & \frac{V_{O_1}+V_{O_2}}{V_i} = \frac{(d+d_1)(d-d_2)}{d_1(d+d_2)} \end{aligned} \tag{3}$$

Eqs. (4) to (7) give the dc solution of the state-space equations for inductor currents, and output voltages and currents.

$$\begin{aligned} & i_{Lm} = V_i \frac{(d+d_1)(d-d_2)^2}{d_1^2(d+d_2)^2(R_{LED1}+R_{LED2})} + \\ & (V_{LED1}+V_{LED2}) \frac{(d_2-d)}{d_1(d+d_2)(R_{LED1}+R_{LED2})} \end{aligned} \tag{4}$$

$$\begin{aligned} & i_{L1} = i_{L2} = V_i \frac{(d+d_1)(d-d_2)}{d_1(d+d_2)^2(R_{LED1}+R_{LED2})} - \\ & (V_{LED1}+V_{LED2}) \frac{1}{(d+d_2)(R_{LED1}+R_{LED2})} \end{aligned} \tag{5}$$

$$\begin{aligned} & V_{O1} = \\ & V_i \frac{(d+d_1)(d-d_2)R_{LED1}}{d_1(d+d_2)(R_{LED1}+R_{LED2})} + \\ & \frac{R_{LED2}V_{LED1}-R_{LED1}V_{LED2}}{(R_{LED1}+R_{LED2})} \end{aligned} \tag{6}$$

$$\begin{aligned} & V_{O2} = \\ & V_i \frac{(d+d_1)(d-d_2)R_{LED2}}{d_1(d+d_2)(R_{LED1}+R_{LED2})} - \\ & \frac{R_{LED2}V_{LED1}+R_{LED1}V_{LED2}}{(R_{LED1}+R_{LED2})} \end{aligned} \tag{7}$$

In the following, the dynamic model of the proposed LED driver is derived and employed in the design of a linear controller, which is developed to simultaneously regulate the output current and the input power factor through the duty cycle ‘d’. Considering variations in the state variables, inputs, outputs, and all terms within the state equations, both dc and ac components naturally appear in the formulation. The parameters through which the system is controlled are also taken into account, and in this paper, the duty cycle ‘d’ is expressed in terms of both its dc and ac components. Each state, input and output variable is expressed as $x(t) = X + \tilde{x}(t)$, where X is the dc operating point and is the small-signal variation [21, 22]. The duty ratio is treated similarly as $d(t) = D + \tilde{d}$. By incorporating both the ac and dc components into the state equations and retaining only the first-order ac terms, the relationship between the input (the system's control parameter) and the output becomes linear, and the ac transfer function of the system is derived as follows:

$$\tilde{x}' = \tilde{A}\tilde{x} + \tilde{B}\tilde{u} \tag{8}$$

The designed controller consists of inner and outer loops. The inner loop controls the inductor current i_{Lm} (input power factor), while the outer loop regulates the output currents i_{O1} and i_{O2}. These two loops are fully described below. To achieve a high-power factor on the grid side and ensure the desired output current, the transfer functions are extracted and the controller is designed accordingly. Variations in the load, input source, and duty cycle ‘d’ cause changes in the state variables. Therefore, by defining the dc and ac components (variations) for each variable and substituting them into Eq. (1), and by considering only the first-order ac terms, the ac steady-state equation is obtained as Eq. (9).

$$\dot{\tilde{\mathbf{x}}} = \mathbf{A}\tilde{\mathbf{x}} + \mathbf{B}\tilde{\mathbf{u}}, \tag{9}$$

where,

$$\tilde{\mathbf{x}} = \begin{bmatrix} \tilde{i}_{Lm} & \tilde{i}_{L1} & \tilde{i}_{L2} & \tilde{v}_{C1} & \tilde{v}_{C2} & \tilde{v}_{O1} & \tilde{v}_{O2} & \tilde{i}_{O1} & \tilde{i}_{O2} \end{bmatrix}^T,$$

and

$$\tilde{\mathbf{u}} = \begin{bmatrix} \tilde{V}_i & \tilde{V}_{LED1} & \tilde{V}_{LED2} & \tilde{d} & \tilde{d}_1 & \tilde{d}_2 \end{bmatrix}^T.$$

The state matrix is partitioned as:

$$\mathbf{A} = \begin{bmatrix} A_{11} & A_{12} & A_{13} \\ A_{21} & A_{22} & A_{23} \\ A_{31} & A_{32} & A_{33} \end{bmatrix},$$

where,

$$A_{11} = \begin{bmatrix} 0 & 0 & 0 \\ 0 & 0 & 0 \\ 0 & 0 & 0 \end{bmatrix},$$

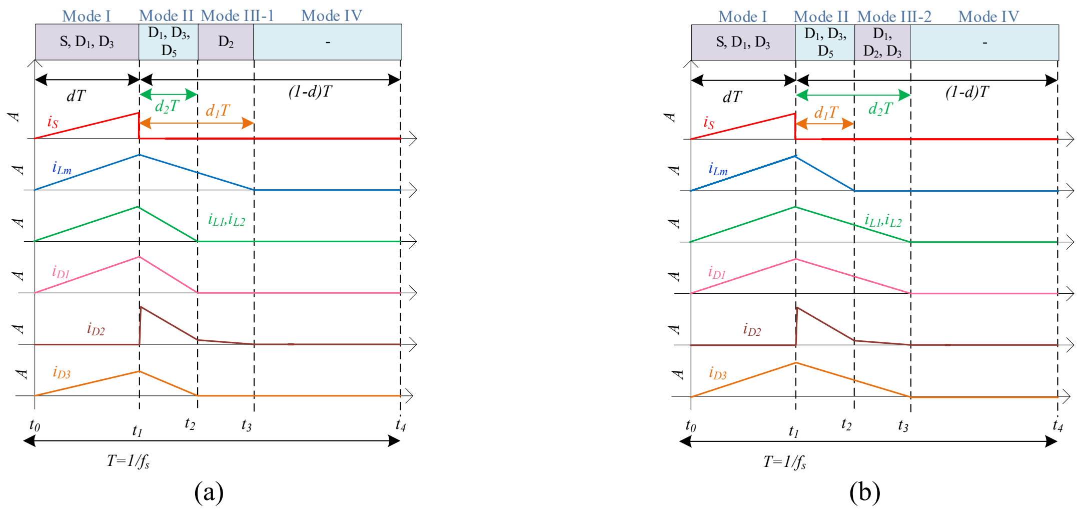

Fig. 3. Main waveforms over a switching interval: (a) Modes I, II, III-1, IV; (b) Modes I, II, III-2, IV.

$$A_{12} = \begin{bmatrix} -\dfrac{d_1}{L_m} & -\dfrac{d_1}{L_m} & 0 \\ \dfrac{d}{L_1} & -\dfrac{d_2}{L_1} & -\dfrac{d+d_2}{L_1} \\ -\dfrac{d_2}{L_2} & \dfrac{d}{L_2} & 0 \end{bmatrix},$$

$$A_{13} = \begin{bmatrix} 0 & 0 & 0 \\ 0 & 0 & 0 \\ -\dfrac{d+d_2}{L_2} & 0 & 0 \end{bmatrix},$$

$$A_{21} = \begin{bmatrix} \dfrac{d_1}{C_1} & -\dfrac{d}{C_1} & \dfrac{d_2}{C_1} \\ \dfrac{d_1}{C_2} & \dfrac{d_2}{C_2} & -\dfrac{d}{C_2} \\ 0 & \dfrac{d+d_2}{C_{O1}} & 0 \end{bmatrix},$$

$$A_{22} = \begin{bmatrix} 0 & 0 & 0 \\ 0 & 0 & 0 \\ 0 & 0 & 0 \end{bmatrix},$$

$$A_{23} = \begin{bmatrix} 0 & 0 & 0 \\ 0 & 0 & 0 \\ 0 & -\dfrac{1}{C_{O1}} & 0 \end{bmatrix},$$

$$A_{31} = \begin{bmatrix} 0 & 0 & \dfrac{d+d_2}{C_{O2}} \\ 0 & 0 & 0 \\ 0 & 0 & 0 \end{bmatrix},$$

$$A_{32} = \begin{bmatrix} 0 & 0 & 0 \\ 0 & 0 & 0 \\ 0 & 0 & 0 \end{bmatrix},$$

$$A_{33} = \begin{bmatrix} 0 & 0 & -\dfrac{1}{C_{O2}} \\ \dfrac{1}{L_{O1}} & -\dfrac{R_{LED1}}{L_{O1}} & 0 \\ 0 & \dfrac{1}{L_{O2}} & -\dfrac{R_{LED2}}{L_{O2}} \end{bmatrix}.$$

Similarly, partition:

$$\mathbf{B} = \begin{bmatrix} B_{11} & B_{12} \\ B_{21} & B_{22} \\ B_{31} & B_{32} \end{bmatrix},$$

with

$$B_{11} = \begin{bmatrix} \dfrac{d+d_1}{L_m} & 0 & 0 \\ 0 & 0 & 0 \\ 0 & 0 & 0 \end{bmatrix},$$

$$B_{12} = \begin{bmatrix} \dfrac{V_i}{L_m} & \dfrac{V_i - V_{C1} - V_{C2}}{L_m} & 0 \\ \dfrac{-V_{O1} + V_{C1}}{L_1} & 0 & -\dfrac{V_{O1} + V_{C2}}{L_1} \\ \dfrac{-V_{O2} + V_{C2}}{L_2} & 0 & -\dfrac{V_{O2} + V_{C1}}{L_2} \end{bmatrix},$$

$$B_{21} = \begin{bmatrix} 0 & 0 & 0 \\ 0 & 0 & 0 \\ 0 & 0 & 0 \end{bmatrix},$$

$$B_{22} = \begin{bmatrix} \dfrac{-i_{L1} + i_{L2}}{C_1} & \dfrac{i_{Lm}}{C_1} & 0 \\ -\dfrac{i_{L2}}{C_2} & \dfrac{i_{Lm}}{C_2} & \dfrac{i_{L1}}{C_2} \\ \dfrac{i_{L1}}{C_{O1}} & 0 & \dfrac{i_{L1}}{C_{O1}} \end{bmatrix},$$

$$B_{31} = \begin{bmatrix} 0 & 0 & 0 \\ 0 & \dfrac{1}{L_{O1}} & 0 \\ 0 & 0 & -\dfrac{1}{L_{O2}} \end{bmatrix},$$

$$B_{32} = \begin{bmatrix} \dfrac{i_{L2}}{C_{O2}} & 0 & \dfrac{i_{L2}}{C_{O2}} \\ 0 & 0 & 0 \\ 0 & 0 & 0 \end{bmatrix}.$$

By substituting Eq. (9) into the $X(S) = \left(SI - \tilde{A}\right)^{-1} \tilde{B}\tilde{U}(S)$, the variations in the output currents and i_{Lm} are derived as follows:

$$\tilde{i}_{O1} = G_{i_{O1}V_i}\tilde{V}_i + G_{i_{O1}V_{LED1}}\tilde{V}_{LED1} +$$
$$G_{i_{O1}V_{LED2}}\tilde{V}_{LED2} + G_{i_{O1}d}\tilde{d} +$$
$$G_{i_{O1}d_1}\tilde{d}_1 + G_{i_{O1}d_2}\tilde{d}_2$$
$$\tilde{i}_{O2} = G_{i_{O2}V_i}\tilde{V}_i + G_{i_{O2}V_{LED1}}\tilde{V}_{LED1} +$$
$$G_{i_{O2}V_{LED2}}\tilde{V}_{LED2} + G_{i_{O2}d}\tilde{d} + \tag{10}$$
$$G_{i_{O2}d_1}\tilde{d}_1 + G_{i_{O2}d_2}\tilde{d}_2$$
$$\tilde{i}_{Lm} = G_{i_{Lm}V_i}\tilde{V}_i + G_{i_{Lm}V_{LED1}}\tilde{V}_{LED1} +$$
$$G_{i_{Lm}V_{LED2}}\tilde{V}_{LED2} + G_{i_{Lm}d}\tilde{d} +$$
$$G_{i_{Lm}d_1}\tilde{d}_1 + G_{i_{Lm}d_2}\tilde{d}_2$$

From Eq. (10), the required conversion functions are obtained as follows:

$$G_{i_{O1}V_i} = \left.\frac{\tilde{i}_{O1}}{\tilde{V}_i}\right|_{\substack{\tilde{d}=0\\ \tilde{d}_1=0\\ \tilde{d}_2=0\\ \tilde{V}_{LED1}=0\\ \tilde{V}_{LED2}=0}} \tag{11}$$

$$G_{i_{O2}V_i} = \left.\frac{\tilde{i}_{O2}}{\tilde{V}_i}\right|_{\substack{\tilde{d}=0\\ \tilde{d}_1=0\\ \tilde{d}_2=0\\ \tilde{V}_{LED1}=0\\ \tilde{V}_{LED2}=0}} \tag{12}$$

$$G_{i_{Lm}d} = \left.\frac{\tilde{i}_{Lm}}{\tilde{d}}\right|_{\substack{\tilde{V}_i=0\\ \tilde{d}_1=0\\ \tilde{d}_2=0\\ \tilde{V}_{LED1}=0\\ \tilde{V}_{LED2}=0}} \tag{13}$$

$$G_{i_{Lm}V_i} = \left.\frac{\tilde{i}_{Lm}}{\tilde{V}_i}\right|_{\substack{\tilde{d}=0\\ \tilde{d}_1=0\\ \tilde{d}_2=0\\ \tilde{V}_{LED1}=0\\ \tilde{V}_{LED2}=0}} \tag{14}$$

Assuming $L_1 = L_2 = L$, $C_1 = C_2 = C$, $LO1 = LO2 = LO$, and $C_{O1} = C_{O2} = C_O$, the conversion function of is given by $G_{i_{O1}V_i}$. By dividing Eqs. (11) and (12) by Eq. (14), the following equations is obtained:

$$G_{i_{O1}i_{Lm}} = \left.\frac{\tilde{i}_{O1}}{\tilde{i}_{Lm}}\right|_{\substack{\tilde{d}=0\\ \tilde{d}_1=0\\ \tilde{d}_2=0\\ \tilde{V}_{LED1}=0\\ \tilde{V}_{LED2}=0}} \tag{15}$$

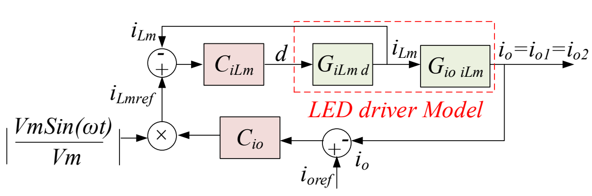

Fig. 4. Block diagram of the linear controller for the proposed LED driver.

Eqs. (14) and (15) are used for controller design. Fig. 4 shows the block diagram of the linear driver controller, where C_{iO} is the output current controller and C_{iLm} is the power factor controller on the ac network side. Both controllers are proportional–integral (PI) controllers.

Using the dc values obtained from Eq. (1) and the component values according to Table 4, the transfer functions of G_{iLmd} and G_{ioiLm} are obtained as Eqs. (16) and (17), which have left-side poles and are stable.

$$G_{i_{Lm}d} = \frac{(s+1582)(s+2481)(s+1274\pm j3526)(s+740\pm j12244)(s+3000000\pm j0.038)}{(s+3000000)^2(s+2453)(s+689\pm j11716)(s+673\pm j3019)(s+747\pm j1073)} \tag{16}$$

$$G_{i_O i_{Lm}} = \frac{(s+3000000)(s+398\pm j4092)(s+2540)}{(s+2455)(s+1202)(s+817\pm j2952)(s+690\pm j11708)(s+3000000\pm j0.052)} \tag{17}$$

In order to achieve the desired power factor and output current, a PI controller has been used in both the inner and outer loops, which have the following conversion functions, in which $T_i = 0.01$ s is selected.

$$C_{i_{Lm}} = k_{i1}(1 + \frac{1}{T_i s}) = k_{i1}(\frac{s+100}{s}) \tag{18}$$

$$C_{i_O} = k_{i2}(1 + \frac{1}{T_i s}) = k_{i2}(\frac{s+100}{s}) \tag{19}$$

By plotting the root locus for $G_{iLmd}C_{iLm}$ and $G_{ioiLm}C_{io}$ shown in Fig. 5 and Fig. 6, to maintain stability, $0 < k_{i1} < \infty$ and $0 < k_{i2} < 10.6$ must be satisfied.

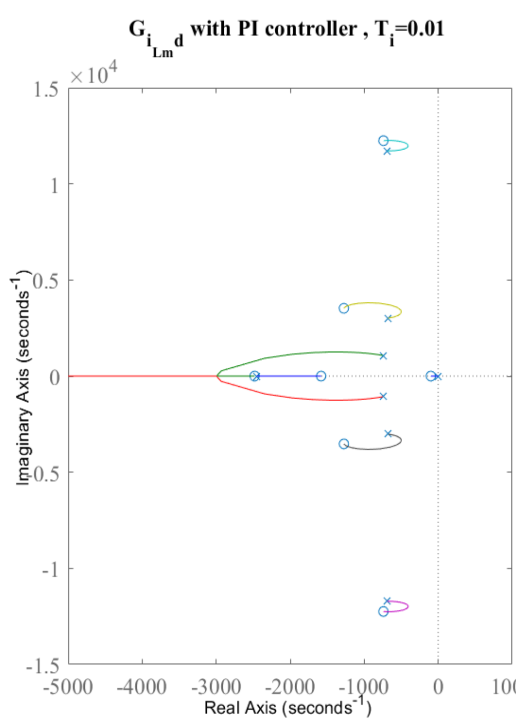

Fig. 5. G_{iLmd} root locus with PI controller.

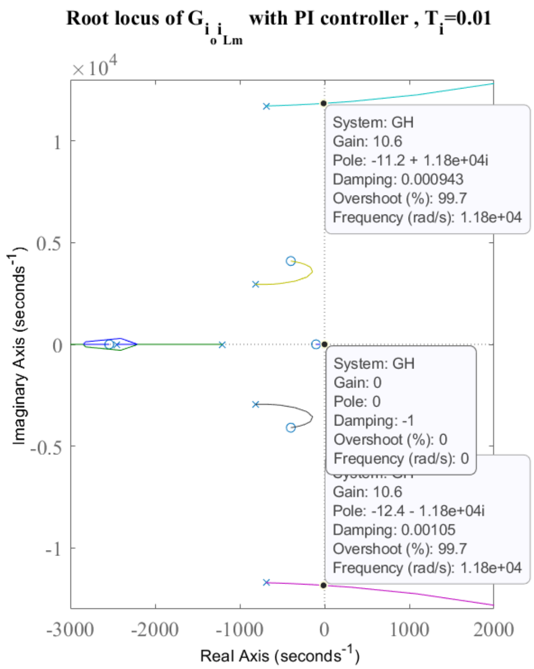

Fig. 6. G_{ioiLm} root locus with PI controller.

4. Loss calculation

There are various methods to assess losses in converters, but initially, it is more appropriate to explain the categories of losses. A converter consists of semiconductor devices such as switches and diodes, along with passive components like inductors and capacitors. For instance, the converter presented in this paper illustrates a dual-output configuration, with these components detailed in Fig. 1. Each of these components experiences losses, which are detailed in this section. Eq. (20) represents the total losses of the converter, encompassing the MOSFET, diodes and inductors losses.

$$P_{loss} = P_{loss-inductors} + P_{loss-S} + P_{loss-Diods} \tag{20}$$

One MOSFET 60F2170 described in Table 4 with On-State Resistance, $r_s = 0.17\ \Omega$, is used in the converter. The average current of MOSFET is calculated in Eq. (21).

$$i_s = i_{Lm} + i_{L2} = V_i \frac{(d+d_1)(d-d_2)(d+d_1-d_2)}{d_1^2(d+d_2)^2(R_{LED1}+R_{LED2})} - (V_{LED1}+V_{LED2})\frac{(d+d_1-d_2)}{d_1(d+d_2)(R_{LED1}+R_{LED2})} \tag{21}$$

Using Eq. (21), the MOSFET conduction loss, P_{loss-S}, is calculated as Eq. (22). The losses incurred during conduction in the transistor arise from the interconnection of semiconductors within the component. These losses are influenced by the manufacturing technology and the operational conditions of the circuit, specifically regarding the power and current flowing through the component. To mitigate these losses, it is possible to decrease the resistance of the junctions during the production process of the component.

$$P_{loss-S} = r_S i_S^2 = r_S\Big(V_i \frac{(d+d_1)(d-d_2)(d+d_1-d_2)}{d_1^2(d+d_2)^2(R_{LED1}+R_{LED2})} - (V_{LED1}+V_{LED2})\frac{(d+d_1-d_2)}{d_1(d+d_2)(R_{LED1}+R_{LED2})}\Big)^2 \tag{22}$$

Three SFF508G 5A, 600V diodes described in Table 4 with On-State Resistance, $r_d = 0.87\ \Omega$, are used in the converter. Using Eqs. (4) and (5), the total diodes conduction loss, $P_{loss-diodes}$, is calculated as Eq. (23).

$$P_{loss-Diodes} = P_{loss-D_1} + P_{loss-D_2} + P_{loss-D_3} \tag{23}$$

Where,

$$P_{loss-D1} = r_d i_{L1}^2 = r_d\Big(V_i \frac{(d+d_1)(d-d_2)}{d_1(d+d_2)^2(R_{LED1}+R_{LED2})} - (V_{LED1}+V_{LED2})\frac{1}{(d+d_2)(R_{LED1}+R_{LED2})}\Big)^2 \tag{24}$$

$$P_{loss-D2} = r_d i_{L1}^2 = r_d\Big(V_i \frac{(d+d_1)(d-d_2)}{d_1(d+d_2)^2(R_{LED1}+R_{LED2})} - (V_{LED1}+V_{LED2})\frac{1}{(d+d_2)(R_{LED1}+R_{LED2})}\Big)^2 \tag{25}$$

$$P_{loss-} = r_d i_{L2}^2 = r_d\Big(V_i \frac{(d+d_1)(d-d_2)}{d_1(d+d_2)^2(R_{LED1}+R_{LED2})} - (V_{LED1}+V_{LED2})\frac{1}{(d+d_2)(R_{LED1}+R_{LED2})}\Big)^2 \tag{26}$$

Each inductor exhibits core losses and winding-resistance (copper) losses. The core loss is specified during manufacturing and is provided by the inductor supplier; it primarily depends on the frequency and the material of the core. Additionally, as the inductor is constructed from twisted wire, the inherent resistance of the wire results in losses when current flows through it. These losses are quantified using Eq. (27) in the proposed converter.

$$P_{loss-inductors} = P_{loss-Lm} + P_{loss-L1} + P_{loss-L2} \tag{27}$$

Where,

$$P_{loss-Lm} = R_{Lm} i_{Lm}^2 = R_{Lm}\Big(V_i \frac{(d+d_1)(d-d_2)^2}{d_1^2(d+d_2)^2(R_{LED1}+R_{LED2})} + (V_{LED1}+V_{LED2})\frac{(d_2-d)}{d_1(d+d_2)(R_{LED1}+R_{LED2})}\Big)^2 \tag{28}$$

$$P_{loss-L1} = R_{Lm} i_{L1}^2 = R_{L1}\Big(V_i \frac{(d+d_1)(d-d_2)}{d_1(d+d_2)^2(R_{LED1}+R_{LED2})} - (V_{LED1}+V_{LED2})\frac{1}{(d+d_2)(R_{LED1}+R_{LED2})}\Big)^2 \tag{29}$$

$$P_{loss-L2} = R_{Lm} i_{L2}^2 = R_{L2}\Big(V_i \frac{(d+d_1)(d-d_2)}{d_1(d+d_2)^2(R_{LED1}+R_{LED2})} - (V_{LED1}+V_{LED2})\frac{1}{(d+d_2)(R_{LED1}+R_{LED2})}\Big)^2 \tag{30}$$

5. Comparison with the prior-art LED drivers

This subsection compares the proposed single-switch dual-string LED driver with recent state-of-the-art LED drivers and integrated AC–DC topologies. Table 3 summarizes both the hardware/component requirements, including the number of switches, diodes, inductors, transformers, electrolytic capacitors, and non-electrolytic capacitors, and the key power-quality and regulation metrics, including power factor, input-current THD, output-current ripple, and peak efficiency. In this comparison, only a single branch (one string) of the proposed driver is considered. The objective of this comparison is to clarify the main merits

Table 3. Comparison of the proposed led driver with recent led drivers.

Topologies	Number of components							PF	THD (%)	R (%)	η(%)@ P [W]
	NSW	ND	NI	NT	NEC	NPC	NS				
[6]	2	2	2	0	0	2	2	0.99	10	4	92.5@45
[11]	1	5	3	0	0	3	3	0.98	4	30	94.06@120
[12]	2	4	2	1	0	2	2	0.99	7.18	4.21	94.5@180
[17]	2	4	2	1	1	2	2	0.99	NR	5	91.4@75
[23]	1	5	2	2	2	3	2	0.99	10	5	92@100
[24]	2	6	2	0	2	1	2	0.99	10.9	20	96.4@42
[25]	1	6	3	1	2	2	2	0.98	9	10	91.5@100
[26]	2	1	1	1	2	0	1	0.99	7	4	93.2@80
[22]	1	5	2	1	0	3	3	0.99	10	15	97@143
Proposed driver	**1**	**2**	**2**	**0**	**0**	**3**	**2**	**0.97**	**5**	**13**	**94.01@110**

N_{SW}: number of switches; N_D: number of diodes; N_I: number of inductors; N_T: number of transformers; N_{EC}: number of electrolytic capacitors; N_{PC}: number of polyester capacitors; N_S: number of stages in integrated structure; *PF*: maximum power factor of the proposed LED driver; *THD*: minimum total harmonic distortion of the input current; R: LED current ripple; η: peak efficiency; *NR*: not reported.

Table 4. Key components of the simulation and prototype.

Device label	Definition
LED	$2 \times 11 \times 5$ W High-Power LED
$D_1 \sim D_3$	SFF508G, 5 A, 600 V
Power switch	MOSFET 60F2170
Bridge rectifier	D15XB 60
C_1, C_2	4.7 μF, 4.7 μF
C_{O1}, C_{O2}	10 μF, 10 μF
L_1, L_2	500 μH
L_m	2 mH
L_f	1 mH
C_f	330 nF
Output power	2×55 W
Output voltage	39 V
Switching frequency	20 kHz

Table 5. Efficiency Performance Under Different Load Conditions for one string at 220 V and 50 Hz.

Percentage of nominal power	V_o [V]	I_o [A]	P_o [W]	P_{input} [W]	Efficiency [%]
25%	38.93	0.35	13.62	16.36	83.22
50%	38.91	0.70	27.23	29.73	91.58
75%	38.89	1.06	41.22	44.55	92.96
100%	38.87	1.42	55.19	58.70	94.01
Average efficiency					**90.44**

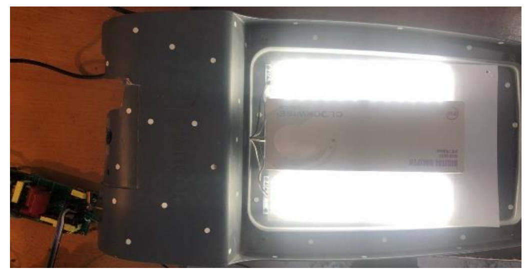

(a)

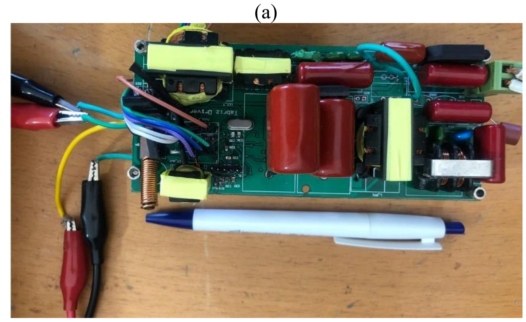

(b)

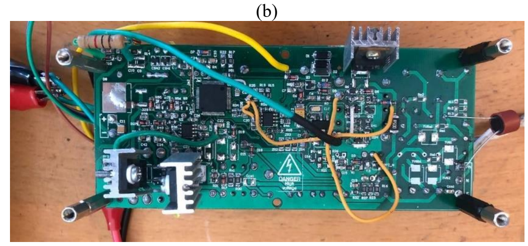

(c)

Fig. 7. Proposed LED driver for industrial-scale applications: (a) Laboratory testing setup, (b) Front view of the prototype, (c) Rear view of the prototype.

of the proposed topology in terms of implementation complexity, performance, and lifetime-oriented design.

A key reliability limitation in offline LED drivers is the electrolytic capacitor, particularly when it is used as the main energy buffer at the rectifier dc-link or as a large output filter element. Although electrolytic capacitors provide high capacitance density and low cost, their service life is typically the shortest among capacitor technologies and degrades significantly at elevated temperatures, which makes them a well-known bottleneck in improving converter lifetime. In contrast, film and ceramic capacitors provide substantially longer service life and superior stability, making them more suitable for long-life luminaires. Consistent with this design objective, Table 3 indicates that the proposed driver does not require any electrolytic capacitor, and the required energy buffering is realized using non-electrolytic capacitors at appropriate circuit nodes. This feature represents a clear advantage over topologies that still employ electrolytic capacitors, such as Ref. [17], and directly supports the long-lifetime positioning of the proposed driver for applications such as street lighting.

From a cost and manufacturability perspective, the number of active devices, gate drivers, and magnetic components strongly affects the overall bill of materials, PCB complexity, and assembly effort. As reported in Table 3, the proposed driver uses only one active switch and does not require a transformer. This

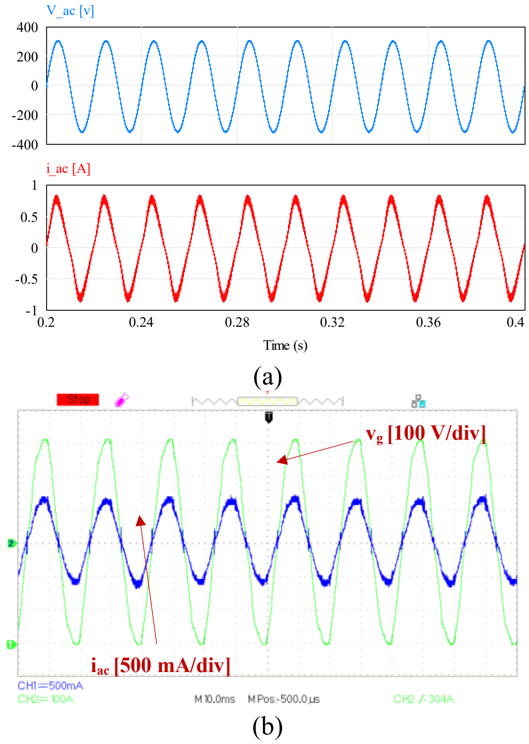

Fig. 8. Input current and grid voltage: (a) Simulation results, and (b) Experimental results.

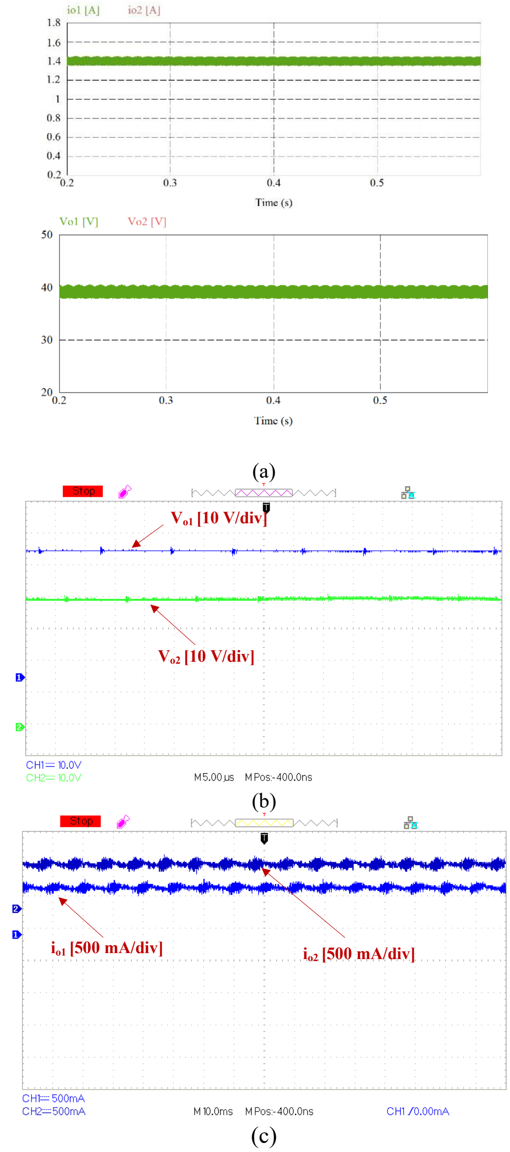

Fig. 9. Voltages and currents at the LED side, (a) Simulation results (b) and (c) Experimental results.

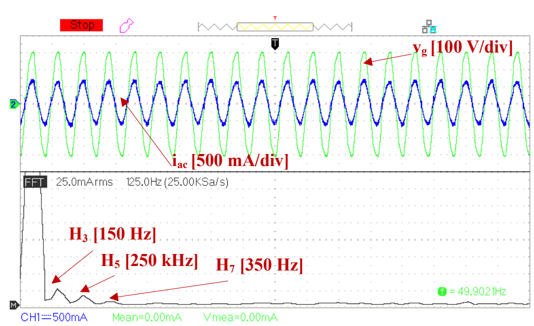

Fig. 10. Fast fourier transform of the input current at a 50Hz grid frequency.

reduces the required gate-driving circuitry and control-interface complexity and also avoids the cost and volume associated with transformer-based solutions. Compared with designs that employ multiple switches and/or transformers, such as Ref. [12] (two switches and one transformer), the proposed structure offers a favorable cost–complexity tradeoff while preserving the intended grid-interface function and regulated LED current delivery.

Regarding power quality and current regulation, grid-connected LED drivers are required to achieve high power factor and low input-current harmonic distortion. Experimental results for the proposed prototype demonstrate PF $\approx$ 0.97 and THD $\approx$ 5%, confirming satisfactory power-quality behavior. Moreover, the proposed driver regulates the LED current with controlled ripple, and Table 3 reports an output-current ripple of 13%. Although some reported topologies achieve lower ripple (e.g., Refs. [6] and [12]), this is typically obtained at the expense of increased hardware complexity, such as additional switches and/or transformer utilization, or by employing different energy-buffering strategies. In addition to the ripple metric, the experimental observations indicate negligible perceptible flicker and compliance with IEEE 1789 recommendations, which supports the suitability of the proposed driver for practical lighting applications. Overall, Table 3 shows that the proposed driver achieves a balanced performance point when benchmarked against Refs. [6], [11], [12], [17]. Relative to Ref. [12], the proposed driver maintains competitive efficiency and satisfactory PF/THD performance while remaining single-switch and transformerless, thereby reducing cost and implementation complexity. Relative to Ref. [17], the proposed driver eliminates electrolytic capacitors and exhibits higher reported efficiency, which strengthens its lifetime-oriented design argument. Relative to Ref. [11], which also follows a single-switch, the proposed driver achieves improved output-current ripple while maintaining high efficiency and acceptable THD. Relative to Ref. [6], which reports lower ripple but uses more switches, the proposed design prioritizes component minimization through a single-switch solution while maintaining competitive PF/THD characteristics.

Finally, beyond these standard power-quality indices, the proposed topology inherently supports dual-string operation with automatic current sharing, and the analytical derivations confirm equal output currents (i_{O1} = i_{O1}), which is a practical advantage for modular

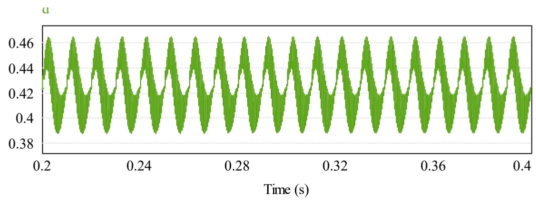

Fig. 11. Summation results of the duty cycle.

and multi-string lighting systems.

6. Simulation and Experimental Evaluation

A 110 W prototype of the proposed LED driver, designed to operate on a 220 V_{rms}, 50Hz AC supply, was developed to validate both simulation and experimental results and to confirm the theoretical analysis. The driver connects eleven 5 W high-power LEDs arranged in two series strings at the output, with each string comprising eleven LEDs in series. Each LED exhibits an ON-state voltage of 0.8 V and a dynamic resistance of 3 Ω. Table 4 provides detailed specifications of the components used in both the simulation and the prototype. Fig. 7 illustrates the industrial-scale LED driver, including the laboratory test setup where the driver is connected to the dual LED strings along with measurement instruments for performance evaluation, as well as front and rear views of the assembled prototype highlighting its key components. The proposed driver supports a wide input voltage range of 180 V_{AC}-265 V_{AC} and delivers a 39 V output at 1.4 A per string, while eliminating electrolytic capacitors to enhance reliability. Furthermore, Fig. 7 shows the layout and placement of both topside and through-hole components, as well as the bottom-side SMD components. The design emphasizes compactness, with overall dimensions of 60 × 140mm and a maximum component height of 25 mm. The PCB is a single-layer FR-4 board, 35 μm thick, accommodating both PTH and SMT components.

Fig. 8-(a) and Fig. 8-(b) show the simulation and experimental waveforms of the input current and the grid voltage. In both scenarios, the input current maintains a nearly perfect sinusoidal shape and remains well synchronized with the grid voltage, demonstrating minimal phase shift. This strong alignment verifies the capability of the proposed LED driver to operate at a near-unity power factor. Furthermore, the waveforms indicate that harmonic distortion in the input current is significantly reduced, ensuring compliance with power quality standards. The close agreement between the simulation and experimental results highlights the accuracy of the modeling approach and the robustness of the control strategy, confirming that the driver can reliably deliver clean current injection into the grid under practical operating conditions.

Fig. 9 presents the simulation and experimental waveforms of the LED-string voltages and output currents, which show a 39V output and an average current of 1.4A per string. In both domains the output currents are regulated to their constant-current setpoints with only a very small superimposed ripple; the low ripple is attributable to the string inductors, the local capacitive filtering and the fast action of the inner current loop. The result is negligible perceptible flicker in the light output. The two output channels also exhibit good current sharing, demonstrating the topology's ability to balance loads without separate current regulators, while the string voltages remain stable around their dc levels despite small dynamic fluctuations. Overall, the combined simulation and experimental evidence validates the topology and control approach for delivering steady, low-ripple current to LED strings while maintaining clean, grid-friendly input current.

Fig. 10 presents the experimental result of the Fast Fourier Transform analysis of the input current waveform under a 50Hz grid frequency. The harmonic spectrum indicates that the 3rd and 5th harmonic components are significantly low, demonstrating the driver's effectiveness in suppressing current harmonics. This result highlights the proposed driver's ability to maintain low total harmonic distortion, comply with grid standards, and provide improved power quality with a near-unity power factor.

Fig. 11 shows the simulated duty-cycle waveform when the designed linear controller is applied to the converter. The trace illustrates the controller's transient action at startup and its response to disturbances (e.g., changes in load or input voltage), where the duty is driven from an initial value to a steady operating point by the cascaded outer–inner loop. In steady state the duty exhibits a small, high-frequency switching ripple superimposed on a low-frequency modulation that carries the current-regulation and power-factor commands; the amplitude and bandwidth of these components reflect the chosen inner/outer loop bandwidth separation and the PWM resolution. The simulation confirms fast disturbance rejection with limited overshoot, bounded duty excursions within the PWM limits and effective anti-windup behavior in the PI regulators, demonstrating the controller's suitability for both regulation and power-factor shaping.

Fig. 12 presents online experimental results recorded by the datalogger for the proposed LED driver under representative operating conditions. Panel (a) shows the grid frequency, while panel (b) plots the output current together with the instantaneous active and reactive powers, illustrating the device's power consumption behavior and the interplay between real and reactive components. Panel (c) reports the measured power factor, 0.97 (lagging), which indicates efficient conversion of input power into useful output with only a small reactive component. Panel (d) shows the input-current total harmonic distortion, measured at approximately 5%, reflecting a largely undistorted current waveform. The harmonic spectrum analysis (also shown) breaks the input-current distortion into individual orders: the third harmonic contributes about 4% and the fifth about 2%, with higher-order components being effectively suppressed.

These measurements demonstrate that the proposed driver achieves low harmonic distortion, a near-unity power factor and stable power consumption, making it well suited for efficient, reliable lighting applications. The results indicate compliance with EN 61000-3-2 Class C harmonic limits. In addition, the driver's flicker performance meets the recommendations of IEEE 1789, and its EMC and safety provisions—together with electrical and thermal protections implemented in the design—support adherence to relevant IEC and UL requirements for street-lighting deployments.

7. Efficiency and performance evaluation

Table 5 summarizes the overall efficiency of the proposed LED driver measured at 220 V, 50 Hz for several load levels. Measurements were performed at 25%, 50%, 75% and 100% of the rated load, and the average efficiency was computed following the ES-2 standard to ensure consistency across operating points. As reported in Table 5, the driver maintains a high and uniform efficiency at the nominal mains voltage, confirming the effectiveness of the topology and component selection in sustaining optimal performance across a wide range of loads and contributing to energy savings and improved system reliability.

Fig. 13 and 14 show simulation results of input, output power and efficiency. Moreover, Fig. 13 shows how the converter efficiency varies with input voltage. The efficiency increases with higher supply voltage, starting at approximately 91% at 180 V_{AC} and rising to about 96% at 260 V_{AC}, where it then remains essentially stable. These results demonstrate that the proposed driver delivers consistently high efficiency over a broad input-voltage range, ensuring reliable operation under diverse supply conditions. As shown in Fig. 15, under nominal test conditions (V_{in} = 220 V, 50 Hz) the measured input power is about 115.8 W

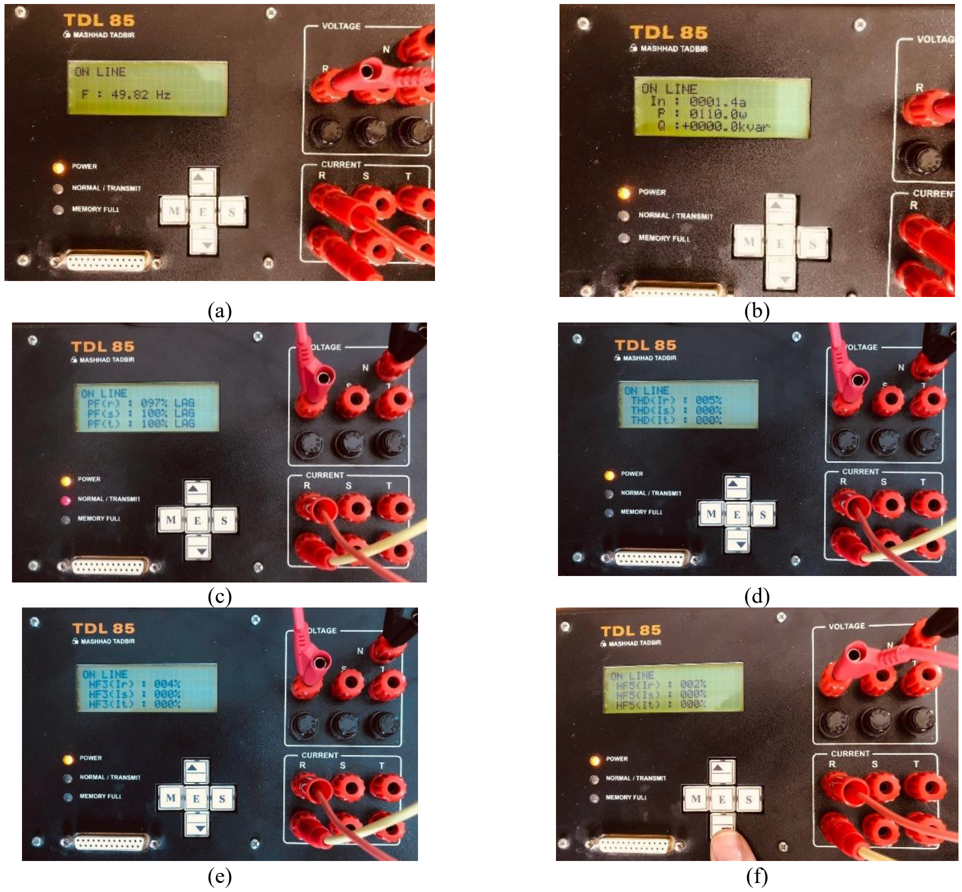

Fig. 12. Datalogger measurements for the proposed LED driver: (a) Grid frequency; (b) Output current with instantaneous active and reactive power; (c) Power factor (PF); (d) Input current total harmonic distortion; (e) and (f) Magnitudes of the 3rd and 5th input-current harmonics.

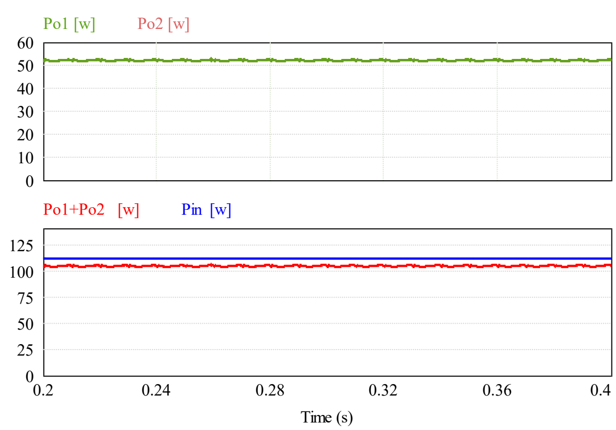

Fig. 13. Simulation results of input and output power.

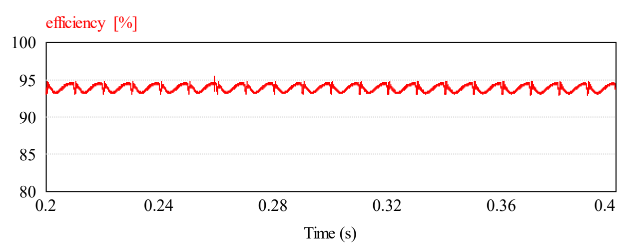

Fig. 14. Simulation results of the Efficiency.

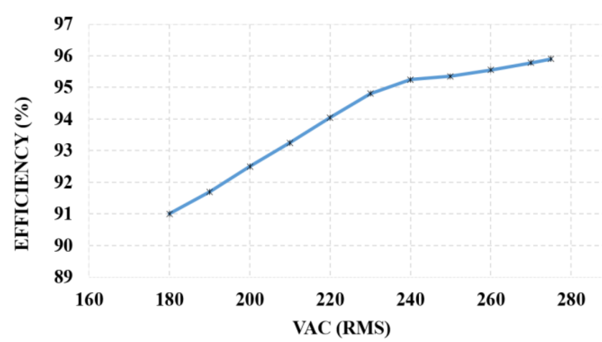

Fig. 15. Efficiency versus input voltage for the test board.

while each output delivers 55.19 W, giving a total output power of 110.38 W. From these measurements the conversion efficiency is calculated as = Pout/Pin ≈ 94.01%, which agrees with the efficiency curve plotted in Fig. 15. The remaining ≈6% (≈7 W) is dissipated as losses, primarily switching and conduction losses in the power semiconductors, copper and core losses in the inductors, and small losses in passive components and measurement circuitry. All measurements were recorded after the board reached thermal steady state; the reported efficiency therefore reflects stabilized operating conditions and is consistent with the broader efficiency trends shown elsewhere in the paper.

8. CONCLUSION

This paper presented a compact single-switch, dual-string, non-isolated constant-current LED driver that integrates boost (PFC) and buck (output regulation) functions into a single switching stage while eliminating large electrolytic dc-link capacitors. A small-signal averaged model was derived and used to design a cascaded inner–outer PI control scheme: the inner loop shapes the magnetizing/line current for high power factor and the outer loops regulate the two string currents. A 110 W prototype (39 V, 1.42 A per string) and complementary simulations validate the concept. Experimental results demonstrate high conversion efficiency (∼94%), near-unity power factor (PF ≈ 0.97, lagging), low input current THD (∼5%) with dominant low-order harmonics, negligible perceptible LED flicker and stable operation over 180–265 V_{AC}. The topology achieves automatic per-string current sharing without separate per-string converters, offering a strong balance between component count, efficiency and reliability for street-lighting applications. Future work will address detailed EMI/EMC testing, elevated-temperature lifetime evaluation, dimming and fault-management features, and adaptive control strategies to further enhance robustness across operating points.

ACKNOWLEDGEMENT

This work was supported by the Department of Electrical Engineering, Tab.C., Islamic Azad University, Tabriz, Iran, and received financial support from Tabriz Electric Power Distribution Company (Contract No. 1402-0008). The authors extend their special thanks to Prof. Mehran Sabahi; Dr. Younes Gharehdaghi (Director of the Research Office at Tabriz Electric Power Distribution Company); Mr. Saeed Abbachizadeh; and Dr. Saeed Razavi for their valuable collaboration and contributions to the successful execution of this project under the aforementioned contract.

ACKNOWLEDGEMENT

The authors acknowledge the use of artificial intelligence tools (e.g., ChatGPT by OpenAI) for language editing and clarity improvement during the preparation of this manuscript. The authors are fully responsible for the scientific content, analysis, and conclusions.

REFERENCES

[1] M. Esteki, S. A. Khajehoddin, A. Safaee, and Y. Li, “LED systems applications and LED driver topologies: A review,” *IEEE Access*, vol. 11, pp. 38324–38358, 2023.

[2] M. Dasohari, N. Vishwanathan, S. Porpandiselvi, and A. R. M. Vani, “A soft-switched boost converter based LED driver with reduced input current ripple,” *IEEE Access*, vol. 12, pp. 45904–45922, 2024.

[3] S. H. Hosseini, M. Sarhangzadeh, and F. Shahnia, “A novel control scheme of the statcom for power quality improvement in electrified railways,” in *Proc. IEEE Power Electron. Spec. Conf.*, 2006.

[4] B. Vakili *et al.*, “Integrated AC/DC converter consisting of three stages for LED driver applications,” *Tabriz J. Electr. Eng.*, vol. 54, no. 1, pp. 87–97, 2024.

[5] K. I. Hwu, J. J. Shieh, and C. T. Lin, “Universal input single-stage high-power-factor LED driver with active low-frequency current ripple suppressed,” *Energies*, vol. 17, no. 1, p. 183, 2024.

[6] R. B. Pallapati and R. Chinthamalla, “Electrolytic capacitor-less reduced power processing single-phase LED driver with power decoupling using split capacitor,” *Int. J. Circuit Theory Appl.*, vol. 51, no. 7, pp. 3118–3145, 2023.

[7] M. Esteki, D. Darvishrahimabadi, M. Shahabbasi, and S. A. Khajehoddin, “An electrolytic-capacitor-less PFC LED driver with low DC-Bus voltage stress for high power streetlighting applications,” *IEEE Trans. Power Electron.*, vol. 38, no. 5, pp. 6294–6310, 2023.

[8] J. F. Ardeshir, A. Ajami, A. Jalilvand, and A. Mohammadpour, “Flexible power electronic transformer for power flow control applications,” *J. Oper. Autom. Power Eng.*, vol. 1, no. 2, pp. 147–155, 2007.

[9] K. A. Kumar and B. L. Narasimharaju, “Performance analysis of a bridgeless power factor correction (PFC) buck–boost LED driver with ripple diversion scheme for extended lifespan,” *Int. J. Circuit Theory Appl.*, vol. 52, no. 8, pp. 3870–3888, 2024.

[10] J. M. Alonso, G. Z. Abdelmessih, M. A. D. Costa, Y. Guan, and Y. Wang, “Investigation of the use of switched capacitor converters as LED drivers,” *IEEE Trans. Ind. Appl.*, vol. 61, no. 1, pp. 1305–1317, 2025.

[11] M. Sarhangzadeh, J. F. Ardashir, and H. K. Jahan, “Non-isolated integrated three-stage LED driver for 120w street lighting application,” in *Proc. 10th Int. Conf. Technol. Energy Manag.*, 2025.

[12] H. L. Cheng, Y. N. Chang, L. C. Hwang, and T. H. Tu, “A single-stage electrolytic-capacitor-free AC-DC LED driver with high power factor and soft switching characteristics,” *IEEE Trans. Power Electron.*, vol. 39, no. 10, pp. 13320–13335, 2024.

[13] S. J. Ji, W. G. Li, J. C. Zhang, A. L. Wang, Y. L. Liang, and G. L. Tong, “Single stage low ripple LED driver power supply without electrolytic capacitor,” in *Proc. 4th Int. Conf. Electr. Eng. Mechatronics Technol.*, pp. 82–86, 2024.

[14] J. F. Ardashir and H. V. Ghadim, “Introduction and literature review of cost-saving characteristics of multi-carrier energy networks,” in *Power Systems*, pp. 1–37, 2021.

[15] J. S. Brand, G. Z. Abdelmessih, J. M. Alonso, Y. Wang, Y. Guan, and M. A. D. Costa, “Capacitance reduction in flicker-free integrated offline LED drivers,” *IEEE Trans. Ind. Electron.*, vol. 68, pp. 11992–12001, Dec. 2021.

[16] S. Mukherjee, V. Yousefzadeh, A. Sepahvand, M. Doshi, and D. Maksimovic, “A two-stage automotive LED driver with multiple outputs,” *IEEE Trans. Power Electron.*, vol. 36, pp. 14175–14186, Dec. 2021.

[17] Q. He, Q. Luo, Y. Wei, and P. Sun, “A variable inductor controlled single-stage AC/DC converter for modular multi-channel LED driver,” *IEEE Trans. Energy Convers.*, vol. 36, pp. 2912–2923, Dec. 2021.

[18] D. Hong and H. Cha, “LED current balancing scheme using current-fed Quasi-Z-source converter,” *IEEE Trans. Power Electron.*, vol. 36, pp. 14187–14194, Dec. 2021.

[19] S. Chen, Y. Chen, B. Zhang, and D. Qiu, “Very-high-frequency resonant dual-channel LED driver with capacitive current balance and low voltage stress on diodes,” *IEEE Trans. Power Electron.*, vol. 38, pp. 15032–15044, Dec. 2023.

[20] H. N. et al., “A dual-color channel design enables low flicker, highly efficient, and cost-effective AC-LEDs,” *IEEE Trans. Electron Devices*, vol. 72, no. 10, pp. 5477–5482, 2025.

[21] M. Sarhangzadeh, S. H. Hosseini, M. B. B. Sharifian, G. B. Gharehpetian, and O. Sarhangzadeh, “Dynamic analysis of DVR implementation based on nonlinear control by IOFL,” in *Proc. Can. Conf. Electr. Comput. Eng.*, pp. 000264–000269, 2011.

[22] B. Vakili, M. Sarhangzadeh, A. Nostratpour, and J. F. Ardashir, “Integrated isolated AC/DC converter using iofl for LED driver applications,” *IEEE Trans. Power Electron.*, vol. 38, pp. 8825–8837, July 2023.

[23] S. Zhang, X. Liu, Y. Guan, Y. Yao, and J. M. Alonso, “Modified zero-voltage-switching single-stage LED driver based on class e converter with constant frequency control method,” *IET Power Electron.*, vol. 11, pp. 2010–2018, Oct. 2018.

[24] A. Malschitzky, E. Agostini, and C. B. Nascimento, "Integrated bridgeless-boost nonresonant half-bridge converter employing hybrid modulation strategy for LED driver applications," *IEEE Trans. Ind. Electron.*, vol. 68, pp. 8049–8060, Sept. 2021.

[25] Y. Wang, J. Huang, W. Wang, and D. Xu, "A single-stage single-switch LED driver based on class-E converter," *IEEE Trans. Ind. Appl.*, vol. 52, pp. 2618–2626, May 2016.

[26] H. Li, S. Li, W. Xiao, and S. Y. R. Hui, "A modulation method for capacitance reduction in active-clamp flyback-based AC-DC adapters," *IEEE Trans. Power Electron.*, vol. 37, pp. 9455–9467, Aug. 2022.